

The comments of RC1

1、 Reply to the comment 1:

1.1 Comments from Referees

The technique used in the data processing is the Full Rank Matrix (FRAM) Small Baseline Subset InSAR (SBAS) time-series analysis, but the method is not clearly described in the main text. More details of the technique should be added in Section 3.2.

1.2 Author's response

According to your suggestion, we will add the details of the technique in section 3.2. As follows:

The main key steps of the FRAM-SBAS (Full Rank Matrix-Small Baseline Subset InSAR) method are:

Firstly, the principle of interferogram generation is based on a specific time base and space baseline, and the appropriate redundant interferogram is selected to maximize the interferogram coherence. The main constraints are

$$\begin{aligned} |\Delta B_{\perp}| &< B_{\perp thr} \\ |\Delta t| &< t_{thr} \\ |\Delta DC| &< DC_{thr} \end{aligned}$$

Where ΔB_{\perp} is the vertical baseline of data interference pairs, Δt is the time baseline and ΔDC is the Doppler frequency difference.

Secondly, selection of coherence points. The coherence point is selected based on the principle of full rank matrix, which effectively improves the quality of coherent point selection and provides the basis for subsequent least squares inversion. By constructing a single set interferogram network, each point can construct the following matrix (Equation 1). Where A is a $M * N$ dimensional matrix, M is the number of interferograms, and N is the number of images. For any pixel in any interferogram, the coherence is greater than a certain threshold, and the -1 and 1 flags can be set at the corresponding positions of the matrix A of Equation 1. For example, the first interferogram consists of the first image and the third image, that is $\delta_{\phi_1} = \phi_3 - \phi_1$. If the interference of a certain point in the interferogram satisfies the condition, the corresponding positions are $A_{11} = -1$ and $A_{13} = 1$, and the remaining positions of the first line are 0. Similarly, the second interferogram, if the coherence of the point in one of the

interferograms is less than the coherence threshold, the diversion is set to zero. All interferograms are judged to obtain each point pair matrix, and then the rank of each matrix is judged. If the matrix is full rank, the point is selected as the coherence point. The method can select coherent points that are coherent in the time series and coherent in the partial time interval but the interference network is connected, thereby increasing the number and precision of the coherent points.

$$A = \begin{bmatrix} -1 & 0 & 1 & \cdots & 0 & 0 & 0 \\ 0 & -1 & 1 & \cdots & 0 & 0 & 0 \\ \cdots & \cdots & \cdots & \cdots & \cdots & \cdots & \cdots \\ 0 & 0 & 0 & \cdots & -1 & 1 & 0 \\ 0 & 0 & 0 & \cdots & -1 & 0 & 1 \end{bmatrix} \quad (1)$$

Thirdly, discrete point phase unwrapping. In the FRAM-SBAS method, discrete coherence point data is resampled onto a regular Cartesian grid, and phase unwrapping is performed using a network flow method. Then, the phase jump is checked by the closed ring residual method, and the jump phase is corrected for the jump region.

Fourthly, orbital and atmospheric error removal. The orbit error removal is performed using the network method proposed by Biggs et al., (2007). The atmospheric error is divided into long-wavelength atmospheric delay error and turbulent atmospheric delay error and terrain-related atmospheric delay error. The three errors are removed using the network methods.

Traditional atmospheric delay phase (APS) estimates are based on a single interferogram (Ferretti et al., 2001). The atmospheric phase in the interferogram is the difference in atmospheric phase delay between the sub-image and the main image. If one of the two images is used to generate other interferograms, the phase delay signal on the image is also passed to the other interferograms, which also makes a correlation between the two interferograms. In this paper, we will use the network method to estimate the atmospheric delay error of each image acquisition time, and then use these estimates to obtain the delay error of a single moment to reconstruct the atmospheric delay error of each interferogram.

After removing the DEM error and the deformation phase, it can be assumed that the residual phase is mainly caused by the atmosphere. Suppose $\delta\varphi_j(x, y)$ represents the residual phase value at (x, y) on the j th interferogram, and $\varphi(t_A, x, y)$ and $\varphi(t_B, x, y)$ represent the phase values of the imaging moments t_A and t_B at (x, y) , respectively. Each interferogram can be expressed by equation (2).

$$\delta\varphi_j(x, y) = \varphi(t_B, x, y) - \varphi(t_A, x, y) \quad (2)$$

Based on a short baseline set network, we can construct equations such as (3)

$$\delta\varphi = A * \varphi \quad (3)$$

Where A represents the $M * N$ matrix. The element A_{kl} of the matrix A is defined according to the following rules: If $l = t_B$, then $A_{kl} = 1$; if $l = t_A$, then $A_{kl} = -1$; otherwise $A_{kl} = 0$. $\delta\varphi$ is a known vector of M dimension, representing the number of interferograms are M ; φ is an N -dimensional unknown vector representing the atmospheric phase values of N imaging moments. Equation (3) can be written as

$$\begin{bmatrix} \delta\varphi_1(x, y) \\ \vdots \\ \delta\varphi_k(x, y) \end{bmatrix} = \begin{bmatrix} -1 & 0 & 1 & & \\ & \ddots & & \ddots & \\ & & & 0 & -1 & 1 \end{bmatrix} \begin{bmatrix} \varphi^{t_0}(x, y) \\ \vdots \\ \varphi^{t_k}(x, y) \end{bmatrix} \quad (4)$$

Where $\delta\varphi_k(x, y)$ represents the residual phase of interferogram k , and the corresponding position is (x, y) .

Since the matrix A is the rank-deficient matrix, a unique solution cannot be obtained. Generally, the singular value decomposition (SVD) method can be used to solve the solution, and the atmospheric delay at each moment is obtained, and then the phase value of each interferogram is simulated by using equation (4). By calculating the variance of the residual phase of each interferogram, if the interferogram has the lowest atmospheric variance, the atmospheric phase of the interferogram is assumed to be zero. This constraint is added to equation (4) to calculate the atmospheric delay phase of all other image acquisition moments (Li Yongsheng, 2014).

Fifthly, the deformation result is obtained. The interference pattern is settled using the least squares method to obtain the deformation results of the study area.

1.3 Author's changes in manuscript.

The contents of the response have been updated to the Section 3.2 (page 4 to page 6).

2、 Reply to the comment 2:

2.1 Comments from Referees

Comment 2: The deformation result from the study is not validated. And what is the precision or accuracy of the derived deformation?

2.2 Author's response

In Section 4.1, the comparison between the results of this paper and the results of others is added, and the reliability of the results is verified. As follows:

In this paper, the SAR data from 2003 to 2012 are analyzed. It is concluded that during the construction of the Qinghai-Tibet Railway, the linear variable along the railway is about 10mm/yr. After the completion of the traffic, the linear variable along the railway is 4~8mm/yr. Li et al., (2012) used SBAS technology to analyze the ENVISAT ASAR data from 1997 to 2010 in the vicinity of Yangbajing-Dangxiong of Qinghai-Tibet Railway. It was found that the settlement rate near the railway was 2mm/yr, and the impact of frozen soil was about 10mm/yr. Zhang et al., (2017) used Sentinel-1 data to analyze the deformation variables of the Qinghai-Tibet Railway during the period of 2014-2016 in the Qinghai-Tibet Plateau. It is concluded that the settlement rate of the Qinghai-Tibet Railway is about -10 mm/yr and the settlement rate of the rail-stabilized area is about -5 mm/yr. Ma et al., (2011) and Dong et al., (2013) analyzed that the overall shape of the Qinghai-Tibet Railway subgrade is <10mm/yr. At the junction of the fracture, we verified it with GPS, which proves that the GPS result is highly consistent with the deformation field acquired by InSAR.

2.3 Author's changes in manuscript.

The contents of the response have been updated to the Section 4.1 (line 5-14 of page 7).

3、 Reply to the comment 3:

3.1 Comments from Referees

Comment 3: The reference style in P2/L1 and the following texts should be rewritten under the style of NHESD, for example, “Xiaolei Lv et al., (2003)” should be changed to “Lv et al., (2003)”.

3.2 Author's response

According to your suggestion, the references formats of the full text have been modified on the basis of your example.

3.3 Author's changes in manuscript.

The contents of the response have been updated to the full manuscript (page 1 to page 9).

4、 Reply to the comment 4:

4.1 Comments from Referees

Comment 4: P3/L7, global positioning systems (GPS) -> Global Positioning Systems (GPS).

4.2 Author's response

According to your suggestion, we changed the global positioning systems (GPS) to Global Positioning Systems (GPS).

4.3 Author's changes in manuscript.

The contents of the response have been updated to the Section 2 (line 10 of page 3).

5、 Reply to the comment 5:

5.1 Comments from Referees

Comment 5: P3/L13-21, Need some references.

5.2 Author's response

According to your suggestion, we will add references in section 2. As follows:

The Qinghai-Tibet Railway is a high-elevation railway that connects Xining (Qinghai Province) to Lhasa (Tibet Autonomous Region) (Figure 1). The Qinghai-Tibet Railway and other national key projects that cross multiple active blocks and faults are vulnerable to earthquakes and other disasters (Chen et al., 2018; Wu et al., 2016). Monitoring the deformation of these projects is of great significance. InSAR and Global Positioning Systems (GPS) are efficient techniques for monitoring the crustal deformation of Qinghai-Tibet blocks (Zhang et al., 2017).

The Qinghai-Tibet Railway, highway, transmission line and other national key projects, with their ancillary studies, have the characteristics of strong correlations and continuous long-distance distributions. We need to understand how to use these features to monitor the deformation of a long linear region and reveal the movement of the Qinghai-Tibet Plateau block patterns with the deformations of these major project networks.

The Lhasa-Nagqu part of the railway is located at the bottom of the southern valley of the Nyainqentanglha Mountain in the central part of the Lhasa block (Jiang et al., 2018). In general, it is

north-trending, and the Qinghai-Tibet highway and Lhasa River pass through the area. Figure 2 shows the study area, and the base map is derived from a digital elevation model (DEM). The terrain in the area is undulating, with the Nyainqentanglha Mountain Range in the northwest, a mountainous area in the southeast, and the Yangbajing-Damxung Basin in the middle of the region (Wu et al., 2018). The terrain is flat, the Qinghai-Tibet Railway and Qinghai-Tibet Highway pass through the basin, and the vegetation along the railway is rich. Wetlands and low-order regions are widely distributed, and the frozen soil in a long part of the area is rich with ice (Li et al., 2012). The study area is in a midlatitude region, and the land types mainly comprise glaciers, snow, bare rock and other land types. In this area, the Bengco fault lies across the railway; therefore, we also need to study whether the movement of the Bengco fault affects the stability of the railway.

5.3 Author's changes in manuscript.

The contents of the response have been updated to the Section 2 (line 7-25 of page 3).

6、 Reply to the comment 6:

6.1 Comments from Referees

Comment 6: P3/L29-P4/9, The tense of these paragraphs should be the past tense.

6.2 Author's response

According to your suggestion, we changed the paragraph tense in section 3.1. As follows:

The TerraSAR-X data were acquired in stripmap mode, with an incidence angle range of 39° - 40° at HH polarization. The potential of the X-band data for detecting higher deformation gradients compared to that of other sensors benefits from high spatial and temporal resolutions. Nevertheless, the coverage of the stripmap mode data was too small to study long linear engineering. Therefore, in this paper, the C-band ASAR data and TerraSAR-X data were used to analyze the stability of the Qinghai-Tibet Railway. The TerraSAR-X data was selected to verify the accuracy of the ASAR T405 data results over the first corner of the railway in Yangbajain and the ASAR T133 data were used to analyze the deformation of the railway near the Nagqu area because the ASAR T405 data could not cover this area completely, and the ASAR T133 data could also verify the accuracy of the ASAR T405 data results over the Nagqu area. The data coverage was shown in Figure 2 with the blue dotted line.

The ASAR T405 data were acquired from August 2003 to September 2010, but there were no data for 2016; therefore, we processed the data in three stages (2003-2005, 2007, and 2008-2010). The ASAR T133 data were acquired from November 2007 to August 2010. The TerraSAR-X data were acquired from December 2011 to November 2012.

6.3 Author's changes in manuscript.

The contents of the response have been updated to the Section 3.2 (line 3-14 of page 4).

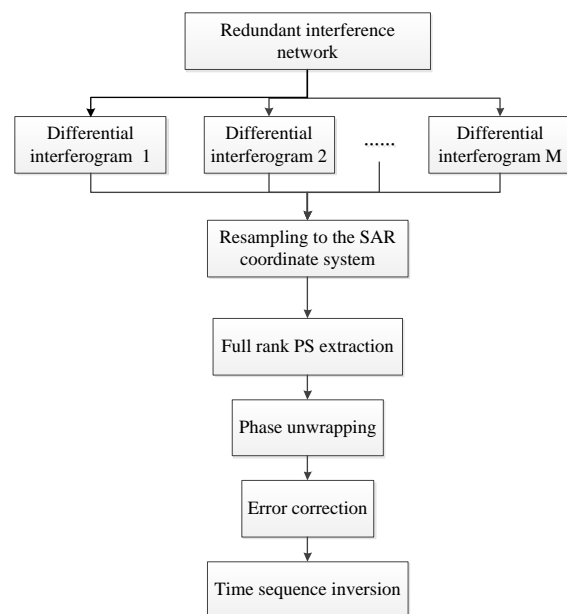
7、 Reply to the comment 7:

7.1 Comments from Referees

In Figure 4, interferograms -> interferogram

7.2 Author's response

According to your suggestion, we changed the interferograms to interferogram in figure 4. As follows:



7.3 Author's changes in manuscript.

The contents of the response have been updated to the figure 4 (page 15).

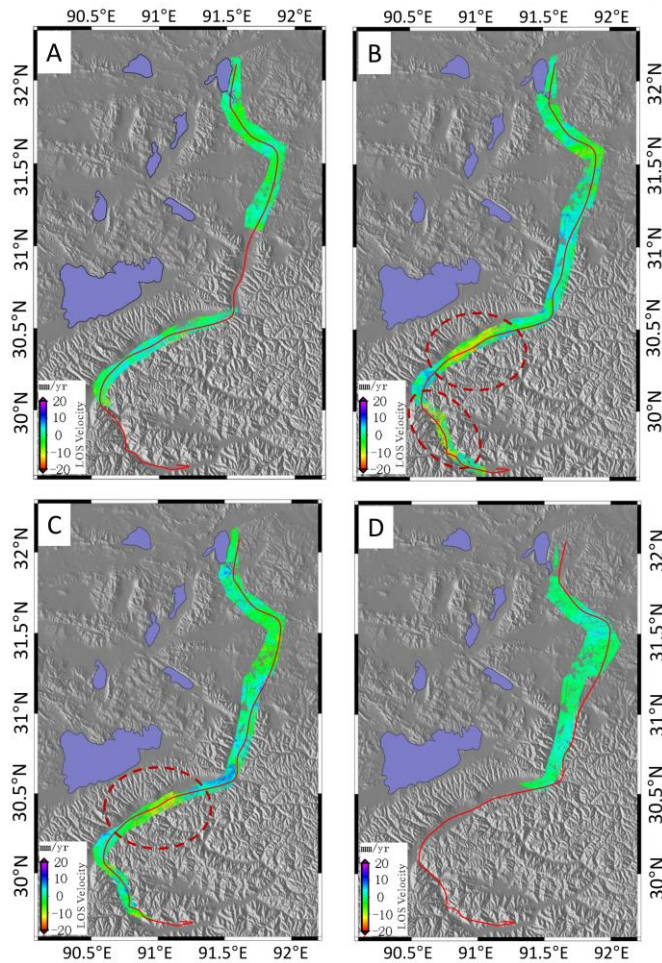
8、 Reply to the comment 8:

8.1 Comments from Referees

Comment 8: The Figures 5, 6 and 7 can be combined as one figure.

8.2 Author's response

According to your suggestion, we combined the figure 5,6 and 7 as figure 5. As follows:



8.3 Author's changes in manuscript.

The contents of the response have been updated to the figure 5 (page 16).

References

- Chen, T., Ma, W., and Zhou, G.: Numerical analysis of ground motion characteristics in permafrost regions along the Qinghai-Tibet Railway, *Cold Regions Science & Technology*, 148, 88-95, <https://doi.org/10.1016/j.coldregions.2018.01.016>, 2018.
- Dong, C. H., and Zhao, X. Q.: Analysis on subgrade deformation features and influence factors in permafrost regions on Qinghai-Tibet Railway, *Railway Standard Design*, 6: 5-8, 2013.
- Jiang, Y., Gao, Y., Dong, Z. B., Liu, B. L., and Zhao, L.: Simulations of wind erosion along the Qinghai-Tibet Railway in north-central Tibet, *Aeolian Research*, 32, 192-201, <https://doi.org/10.1016/j.aeolia.2018.03.006>, 2018.
- Li, S. S.: The study of using SBAS to monitor the Motion of the frozen soil along Qinghai-Tibet railway, Central south university, 2012
- Ma, W., Liu, D., and Wu, Q. B.: Monitoring and analysis of embankment deformation in permafrost regions of Qinghai-Tibet Railway, *Rock Mechanics*, 29(3) : 571-580, 2008.

Ma, W., Mu, Y. H., and Wu, Q. B.: Characteristics and mechanisms of embankment deformation along the Qinghai-Tibet Railway in permafrost regions, *Cold Regions Science and Technology*, 67(3) : 178-186, 2011.

Wu, Z. J., Ma, W., Chen, T., and Wang, L.: Dynamic Stability Analysis of Embankment Along the Qinghai-Tibet Railroad in Permafrost Regions, *Environmental Vibrations and Transportation Geodynamics*, 757-766, Doi: 10.1007/978-981-10-4508-070, 2016.

Zhang, Z. J.: Research on Qinghai-Tibet Permafrost Environment and Engineering using High Resolution SAR Images, Institute of Remote Sensing and Digital Earth, Chinese Academy of Science, 2017.

The comments of RC2

1、 Reply to the comment 1:

1.1 Comments from Referees

Comment 1: I would like to suggest the authors add a short description of the used methodology with a particular emphasis on the estimation and removal of APS.

1.2 Author's response

According to your suggestion, we will add the details of the technique in section 3.2. As follows:

Traditional atmospheric delay phase (APS) estimates are based on a single interferogram (Ferretti et al., 2001). The atmospheric phase in the interferogram is the difference in atmospheric phase delay between the sub-image and the main image. If one of the two images is used to generate other interferograms, the phase delay signal on the image is also passed to the other interferograms, which also makes a correlation between the two interferograms. In this paper, we will use the network method to estimate the atmospheric delay error of each image acquisition time, and then use these estimates to obtain the delay error of a single moment to reconstruct the atmospheric delay error of each interferogram.

After removing the DEM error and the deformation phase, it can be assumed that the residual phase is mainly caused by the atmosphere. Suppose $\delta\varphi_j(x, y)$ represents the residual phase value at (x, y) on the j th interferogram, and $\varphi(t_A, x, y)$ and $\varphi(t_B, x, y)$ represent the phase values of the imaging moments t_A and t_B at (x, y) , respectively. Each interferogram can be

expressed by equation (2).

$$\delta\varphi_j(x, y) = \varphi(t_B, x, y) - \varphi(t_A, x, y) \quad (2)$$

Based on a short baseline set network, we can construct equations such as (3)

$$\delta\varphi = A * \varphi \quad (3)$$

Where A represents the $M * N$ matrix. The element A_{kl} of the matrix A is defined according to the following rules: If $l = t_B$, then $A_{kl} = 1$; if $l = t_A$, then $A_{kl} = -1$; otherwise $A_{kl} = 0$. $\delta\varphi$ is a known vector of M dimension, representing the number of interferograms are M ; φ is an N -dimensional unknown vector representing the atmospheric phase values of N imaging moments. Equation (3) can be written as

$$\begin{bmatrix} \delta\varphi_1(x, y) \\ \vdots \\ \delta\varphi_k(x, y) \end{bmatrix} = \begin{bmatrix} -1 & 0 & 1 & & \\ & \ddots & \ddots & & \\ & & & 0 & -1 & 1 \end{bmatrix} \begin{bmatrix} \varphi^{t_0}(x, y) \\ \vdots \\ \varphi^{t_k}(x, y) \end{bmatrix} \quad (4)$$

Where $\delta\varphi_k(x, y)$ represents the residual phase of interferogram k , and the corresponding position is (x, y) .

Since the matrix A is the rank-deficient matrix, a unique solution cannot be obtained. Generally, the singular value decomposition (SVD) method can be used to solve the solution, and the atmospheric delay at each moment is obtained, and then the phase value of each interferogram is simulated by using equation (4). By calculating the variance of the residual phase of each interferogram, if the interferogram has the lowest atmospheric variance, the atmospheric phase of the interferogram is assumed to be zero. This constraint is added to equation (4) to calculate the atmospheric delay phase of all other image acquisition moments (Li Yongsheng, 2014).

1.3 Author's changes in manuscript.

The contents of the response have been updated to the Section 3.2 (line 1-25 of page 6).

2、 Reply to the comment 2:

2.1 Comments from Referees

Comment 2: Some minor changes are required concerning English style.

2.2 Author's response

According to your suggestion, when the next manuscript is uploaded, the English style of the full text will be revised.

2.3 Author's changes in manuscript.

The contents of the response have been updated to the full-text.

3、 Reply to the comment 3:

3.1 Comments from Referees

Comment 3: Reference to the literature is not adequate but it must be improved by searching for the most recent publications on the InSAR field. Also, the original SBAS paper of Berardino et al. has not been cited. Also, several other SBAS-like methods have been designed and presented in the literature.

3.2 Author's response

According to your suggestion, we will add the reference of the InSAR and SBAS. As follows:

In view of the drawbacks of D-InSAR technology affected by the temporal baseline and spatial displacement, many scholars have proposed new technologies such as InSAR Time Series Analysis Method, to obtain better settlement detection results. The main time series analysis methods of InSAR include Permanent Scatter Interferometry InSAR (PS-InSAR) method (Ferretti et al., 2000, 2001; Rosi et al., 2017; Yang et al., 2018), Small Baseline Subset InSAR (SABS-InSAR) method (Berardino et al., 2002; Dong et al., 2014; Li et al., 2015; Corsetti et al., 2018) and Stacking method (Lundgren et al., 2001; Chang et al., 2011; Dai et al., 2018).

Reference:

Ferretti, A.: Nonlinear subsidence rate estimation using permanent scatterers in differential SAR interferometry, *IEEE Transactions on Geoscience & Remote Sensing*, 38(5), 2202-2212, doi: 10.1109/36.868878, 2000.

Ferretti, A.: Permanent scatterers in SAR interferometry, *IEEE Transactions on Geoscience & Remote Sensing*, 39 (1), 8-20, doi: 10.1109/36.898661, 2001.

Rosi, A., Tofani, V., Tanteri, L., Tacconi, S. C., Agostini, A., Catani, F., and Casagli, N.: The new landslide inventory of Tuscany (Italy) updated with PS-InSAR: geomorphological features and landslide distribution, *Landslides*, 15(1), 5-19, doi: 10.1007/s10346-017-0861-4, 2017 .

Yang, C., Lu, Z., Zhang, Q., Zhao, C. Y., Peng, J. B., and Ji, L. Y.: Deformation at longyao ground fissure and its surroundings, north China plain, revealed by ALOS PALSAR PS-InSAR, *International Journal of Applied Earth Observation and Geoinformation*, 67, 1-9, <https://doi.org/10.1016/j.jag.2017.12.010>, 2018.

Berardino, P., Fornaro, G., Lanari, R., and Sansosti, E.: A New Algorithm for Surface Deformation Monitoring Based on Small Baseline Differential SAR Interferograms, *Geoscience and Remote Sensing, IEEE Transactions*, 40(11), 2375-2383, doi: 10.1109/TGRS.2002.803792, 2002.

Corsetti, M., Fossati, F., Manunta, M., and Marsella, M.: Advanced SBAS-DInSAR technique for controlling large civil infrastructures: An Application to the Genzano di Lucania Dam, *Sensors*, 18(7), doi: 10.3390/s18072371, 2018.

Dong, . (2014). Time-series analysis of subsidence associated with rapid urbanization in shanghai, china measured with sbas insar method. *Environmental Earth Sciences*, 72(3), 677-691.

Dong S. C., Samsonov, S., Yin, H. W., Ye, S. J., and Cao, Y. R.: Time-series analysis of subsidence associated with rapid urbanization in Shanghai, China measured with SBAS InSAR method, *Environmental Earth Sciences*, 72(3), 677-691, doi: 10.1007/s12665-013-2990-y, 2014.

Lundgren, P., Usai, S., Sansoti, E., Lanari, R., Tesauro, M., Fornaro G., and Berardino, P.: Modelling surface deformation observed with synthetic aperture radar interferometry at Campi Flegrei caldera, *Journal of Geophysical Research*, 106 (B9), 19355–19366, doi: 10.1029/2001jb000194, 2001.

Chang, Z. Q., Liu, X. M., Xue, T. F., and Yang, R. R.: Investigating ground subsidence in Beijing by using interferogram stacking InSAR, *IEEE International Conference on Spatial Data Mining & Geographical Knowledge Services*, IEEE, doi: 10.1109/ICSDM.2011.5969068, 2011.

Dai, K. R., Liu, G. X., Li, Z. H., Ma, D. Y., Wang, X. W., Zhang, B., Tang, J., and Li, G. Y.: Monitoring Highway Stability in Permafrost Regions with X-band Temporary Scatterers Stacking InSAR, *Sensors*, 18(6), 1-17, doi: 10.3390/s18061876, 2018.

3.3 Author's changes in manuscript.

The contents of the response have been updated to the Section 1 and the References (line 1-4 of page 2 and page 10-13).